Murine cardiac images obtained with focusing pinhole SPECT are barely influenced by extra-cardiac activity

Murine cardiac images obtained with focusing pinhole SPECT are barely influenced by extra-cardiac activity

Woutjan Branderhorst[1,2,5]**, Frans van der Have**[3,4]**,**
Brendan Vastenhouw[3,4]**, Max A Viergever**[1] **and Freek J Beekman**[1,2,3,4]

[1] Image Sciences Institute University Medical Centre Utrecht, The Netherlands
[2] Rudolf Magnus Institute of Neuroscience, University Medical Centre Utrecht, The Netherlands
[3] Molecular Imaging Laboratories BV, Utrecht, The Netherlands
[4] Section of Radiation Detection and Medical Imaging, Applied Sciences, Delft University of Technology, The Netherlands

E-mail: woutjan@isi.uu.nl

Abstract

Ultra-high-resolution SPECT images can be obtained with focused multipinhole collimators. Here we investigate the influence of unwanted high tracer uptake outside the scan volume on reconstructed tracer distributions inside the scan volume, for ^{99m}Tc-tetrofosmin myocardial perfusion scanning in mice. Simulated projections of a digital mouse phantom (MOBY) in a focusing multipinhole SPECT system (U-SPECT-II, MILabs, The Netherlands) were generated. With this system differently sized user-defined scan volumes can be selected, by translating the animal in 3D through the focusing collimators. Scan volume selections were set to (i) a minimal volume containing just the heart, acquired without translating the animal during scanning, (ii) a slightly larger scan volume as is typically applied for the heart, requiring only small XYZ translations during scanning, (iii) same as (ii), but extended further transaxially, and (iv) same as (ii), but extended transaxially to cover the full thorax width (gold standard). Despite an overall negative bias that is significant for the minimal scan volume, all selected volumes resulted in visually similar images. Quantitative differences in the reconstructed myocardium between gold standard and the results from the smaller scan volume selections were small; the 17 standardized myocardial segments of a bull's eye plot, normalized to the myocardial mean of the gold standard, deviated on average 6.0%, 2.5% and 1.9% for respectively the minimal, the typical and the extended scan volume, while maximum absolute deviations were respectively 18.6%, 9.0% and 5.2%. Averaged over ten low-count noisy simulations, the mean absolute deviations were respectively 7.9%, 3.2% and 1.9%. In low-count noisy simulations, the mean and maximum absolute deviations for the minimal scan volume could be reduced to respectively 4.2% and 12.5% by performing a short survey scan

[5] Author to whom any correspondence should be addressed.

of the exterior activity and focusing the remaining scan time at the organ of interest. We conclude that reconstructed tracer distribution in the myocardium can be influenced by activity in surrounding organs when a too narrow scan volume is used. With slightly larger scan volumes this problem is adequately suppressed. This approach produced a smaller mean deviation and may be more effective than employing a narrow scan volume with an additional survey scan.

(Some figures may appear in colour only in the online journal)

1. Introduction

Molecular imaging has proven to be very valuable in studying human disease and development of new pharmaceuticals and tracers (Pysz *et al* 2010, Massoud and Gambhir 2003, Hoffman and Gambhir 2007). With the goal of translation to clinical medicine, radionuclide techniques such as single photon emission computed tomography (SPECT) and positron emission tomography (PET) can be used to quantitatively study many molecular mechanisms in small animals (King *et al* 2002, Rowland and Cherry 2008, Franc *et al* 2008, Golestani *et al* 2010, Tsui and Kraitchman 2009). Over the past decade, small-animal SPECT has undergone rapid development and improvements in performance (Meikle *et al* 2005, Beekman and van der Have 2007). In particular, spatial resolution has reached the subhalf-millimeter range, using multipinhole collimators exploiting high magnification factors (Beekman *et al* 2005, van der Have *et al* 2009), while high quantitative accuracy has been reached (Wu *et al* 2010, Vanhove *et al* 2009, 2010).

Strong increase of multipinhole sensitivity in SPECT in organs or tumours can be reached when pinholes are focused on a central scan volume (e.g. Beekman *et al* 2005, van der Have *et al* 2009, Funk *et al* 2006a, DiFilippo 2008, Vunckx *et al* 2009, Shokouhi *et al* 2009). Such multipinhole geometries, with pinholes focused on a relatively small central scan volume, can also be used to scan larger volumes—up to total body imaging (Vastenhouw and Beekman 2007). Count yield from a specific organ or a tumour can be increased by confining the scan volume to the region that contains the tissue of interest (Branderhorst *et al* 2010, Beekman *et al* 2005, Vastenhouw *et al* 2007). Special tools for targeting the focus accurately to tissues of interest have been proposed in Branderhorst *et al* (2010) and Baiker *et al* (2009).

In many cases, a consequence of truncating projections is artefacts that can appear in both analytical and iterative SPECT image reconstruction (Zeng and Gullberg 1990, Lalush and Tsui 2000, Xiao *et al* 2010, Gregoriou *et al* 1995). However, in some circumstances it has been shown that if truncated projections sample a small region-of-interest (ROI) sufficiently, that ROI can still be reconstructed accurately (Clackdoyle and Defrise 2010). Some evidence suggests that iterative reconstruction methods can recover larger ROIs than analytic algorithms (Clackdoyle *et al* 2004), and that they can provide reliable reconstructions for some truncation situations where traditional analytical methods fail (Manglos *et al* 1993, Kadrmas *et al* 1995, Zhang and Zeng 2007). However, quantification of the uptake inside an iteratively reconstructed ROI in SPECT may contain a bias depending on the amount of activity that is present outside the ROI (Zeng *et al* 2010, Maass 1992). A general theory for how much a reconstruction from truncated pinhole projections will be quantitatively affected has not been established yet. The aim of the present paper is to investigate empirically how severely focused multipinhole cardiac mouse SPECT scans are affected by truncation.
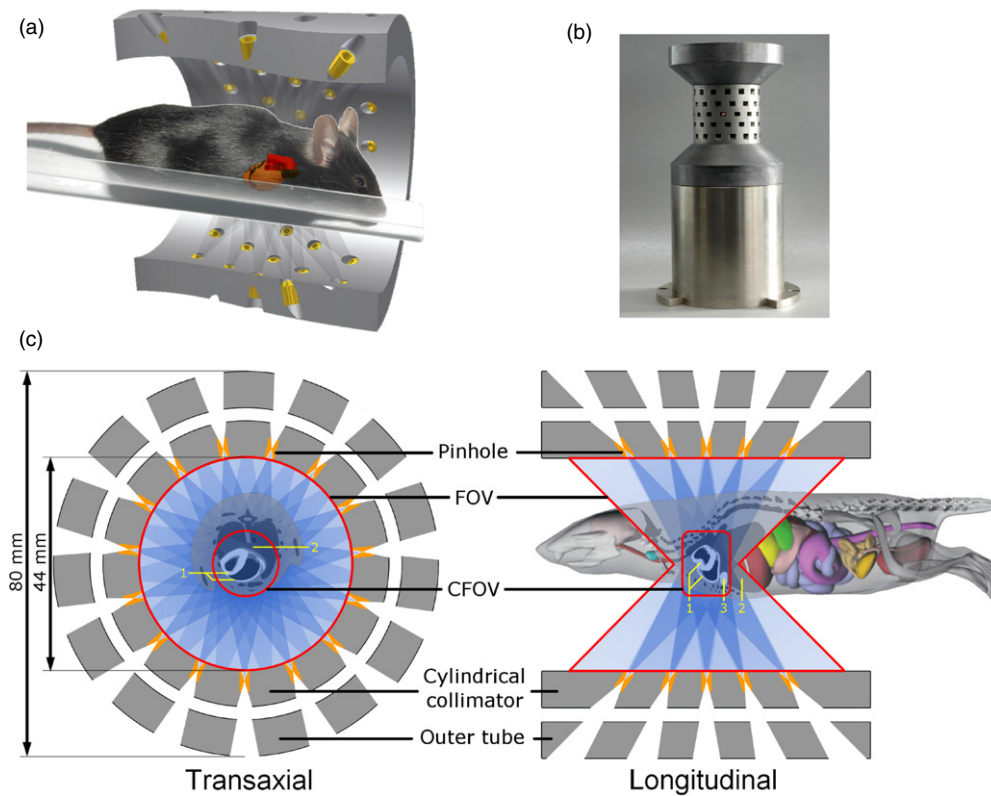
Figure 1. (a) Three-dimensional illustration of simulated general-purpose mouse collimator with heart in focus area of collimator. (b) Collimator with outer shielding tube that avoids overlapping projections on the detector. (c) Schematic cross sections of field-of-view (FOV) and central-field-of-view (CFOV) in simulated collimator, showing how MOBY phantom is truncated in various pinhole projections (1: myocardium, 2: liver, 3: gallbladder).

2. Methods

Simulations of a digital mouse phantom were performed in a focusing multipinhole SPECT system. The use of a digital phantom enables the emulation of activity distributions with realistic organ shapes, in which the uptake concentrations can be easily changed. This section first explains the simulated SPECT system. Next, details are provided on how the projection data and the phantom were generated. Then the reconstruction and analysis of the images are described.

2.1. Multipinhole SPECT system

The simulations were based on the geometry of the U-SPECT-II (van der Have *et al* 2009), a multipinhole SPECT scanner for imaging rodents. It employs a stationary detector array with exchangeable collimators for differently sized animals or for specific organs (van der Have *et al* 2009, Beekman *et al* 2009). In this study, we simulated a mouse collimator consisting of a tungsten cylinder with 75 pinhole apertures (0.6 mm) that together observe a field-of-view (FOV) of which the shape is illustrated in figures 1(a) and (c). The pinhole geometry is chosen

such that the region observed through all pinholes simultaneously is located in the centre of the collimator. For this relatively small part of the entire FOV and a small margin around it, together referred to as the central field of view (CFOV, figure 1(c)), complete data acquisition is obtained without translation of the bed. In the U-SPECT-II general-purpose mouse collimator, the region observed through almost all pinholes simultaneously, and therefore providing complete data, is approximately a cylinder of length 7.5 mm and diameter 12 mm. In addition, an outer tube with square holes is used (figures 1(b) and (c)), which results in trapezium-shaped gamma radiation beams. Both the inner and the outer tubes are made of tungsten (thickness of each tube is 7.5 mm).

The combination of the cylindrical collimator and the outer tube determines the truncation, which is illustrated in figure 1(c). A transaxial cross section through the central ring of pinholes is shown together with a representative longitudinal cross section, which slightly deviates from reality since the pinhole positions in the rings are rotated $8°$ as opposed to each other (figures 1(a) and (b) (Beekman 2004)). Pinholes in the second and fourth ring are tilted by $18°$ and in the outer rings by $34°$. From figure 1(c) it is clear that activity from parts of organs such as the liver and gallbladder can be projected through some but not all pinholes.

Activity outside the CFOV also contributes to the projection data, but in order to obtain complete data from a volume that is significantly larger than the CFOV, the system automatically translates the focus over the pre-selected volume of interest using a motor-controlled XYZ stage (Branderhorst *et al* 2010). Using multiple bed positions is the standard procedure with a U-SPECT system and the effect of the FOV size on the signal-to-noise ratio has been investigated in Branderhorst *et al* (2010). Since the movements can be done very quickly, fast dynamic and gated imaging is possible even for total body imaging (Vaissier *et al* 2010).

2.2. Phantom

The MOBY digital mouse phantom (Segars *et al* 2004) was used as a realistic model of a laboratory mouse. For this study, the MOBY phantom was adapted to also incorporate the gallbladder. The phantom was resized to 0.89 times the default size, such that the resulting mouse model had a heart that has average dimensions for mature C57BL/6 mice (Wiesmann *et al* 2001). Activity uptake in the various phantom organs was set corresponding to the biodistribution reported by Amano *et al* (1998), who estimated the average ^{99m}Tc-tetrofosmin concentration per organ at 3 h after injection based on gamma well counter measurements for five BALB/c nude mice. Relative tracer uptake concentration ratios between the heart and other organs were set equal to the ratios between the %ID g^{-1} values measured by Amano *et al*. Since no studies could be found reporting reliable data on ^{99m}Tc-tetrofosmin uptake in the gall bladder, we estimated the gallbladder/heart ratio from a volume of interest (VOI) analysis in three previously acquired ^{99m}Tc-tetrofosmin mouse myocardial perfusion scans, which were performed in accordance with international guidelines on handling laboratory animals under approval by the local ethical committee. To prevent segmentation inaccuracies due to motion of the heart, the gallbladder/heart ratio was obtained indirectly by measuring the gallbladder/liver ratio. The resulting biodistribution is listed in table 1. Uptake in all non-mentioned organs was assumed to be uniformly distributed, with the same concentration as set for muscle tissue. The phantom was generated on a 0.09375 mm isotropic voxel grid. Three lesions were introduced into the left ventricular myocardium, one in each of the apical, mid- and basal regions. These lesions, affecting respectively 1.3, 1.7 and 2.3 μl of myocardial tissue, were modelled as pie-shaped wedges in which all myocardial voxels were reduced to 40% of the normal myocardial uptake.

Table 1. Tracer uptake concentration relative to heart for various tissues in phantom.

Ratio	Value
Liver/heart	0.16
Gallbladder/heart	7.63
Intestine/heart	2.26
Lung/heart	0.11
Kidney/heart	0.71
Spleen/heart	0.06
Stomach/heart	0.94
Blood/heart	0.04
Bone/heart	0.11
Muscle/heart	0.34

2.3. Scan volume selections

To study the influence of truncation, the following scan volume selections were tested: (i) minimal: a minimal volume containing just the heart, acquired without translating the animal during scanning; (ii) typical: a slightly larger scan volume as is typically used for imaging the heart, requiring only small XYZ translations during scanning; (iii) extended: same as (ii), but extended slightly in the transaxial directions; and (iv) maximal: same as (ii), but extended maximally in the transaxial directions, covering the full thorax width. As the scan volume selection is extended, some otherwise truncated parts become sampled by the CFOV, which decreases the level of truncation. The resulting CFOV locations for each of the scan protocols are shown in figure 2(a), ordered by increasing level of truncation. Figure 2(b) shows an additional scan protocol, which is similar to the minimal scan protocol but sacrifices 18% of the scan time to perform a short survey scan that samples most of the truncated activity. During image reconstruction, the projections are weighted according to the time spent in the corresponding bed positions. Figure 3 shows an example result from a real ^{99m}Tc-tetrofosmin scan in which a typical scan volume with four CFOV positions was employed, similar to the typical volume shown in figure 2.

2.4. Simulation of acquisitions

Emission projection data from the digital phantom were simulated using the system matrix. Because the system matrix was derived from a large series of point-spread-function (PSF) measurements (van der Have *et al* 2008), it includes the effects of distance-dependent detector and pinhole response including pinhole edge penetration. The activity in the phantom was scaled such that the total number of counts simulated for the minimal FOV selection was approximately equal to that obtained in the 3D-targeted scan described in Branderhorst *et al* (2010), for which 134 MBq ^{99m}Tc-tetrofosmin was injected and the scan duration was 45 min. From the resulting activity distribution, emission projection data were generated using each of the five FOV selections. Simulations were performed with and without addition of Poisson-distributed random noise to the generated emission data. Since the aim was to study the effects of projection truncation, noise fluctuations in the noisy data sets were suppressed by generating ten different noise realizations for each simulation and averaging over the results. All simulations were also repeated using a low-count phantom, which was created by downscaling the activity in the high-count phantom by a factor of four, representing a fourfold reduction in injected dose or scan duration. Translation of the XYZ stage was simulated by positioning the phantom at different locations within the support of the system matrix and
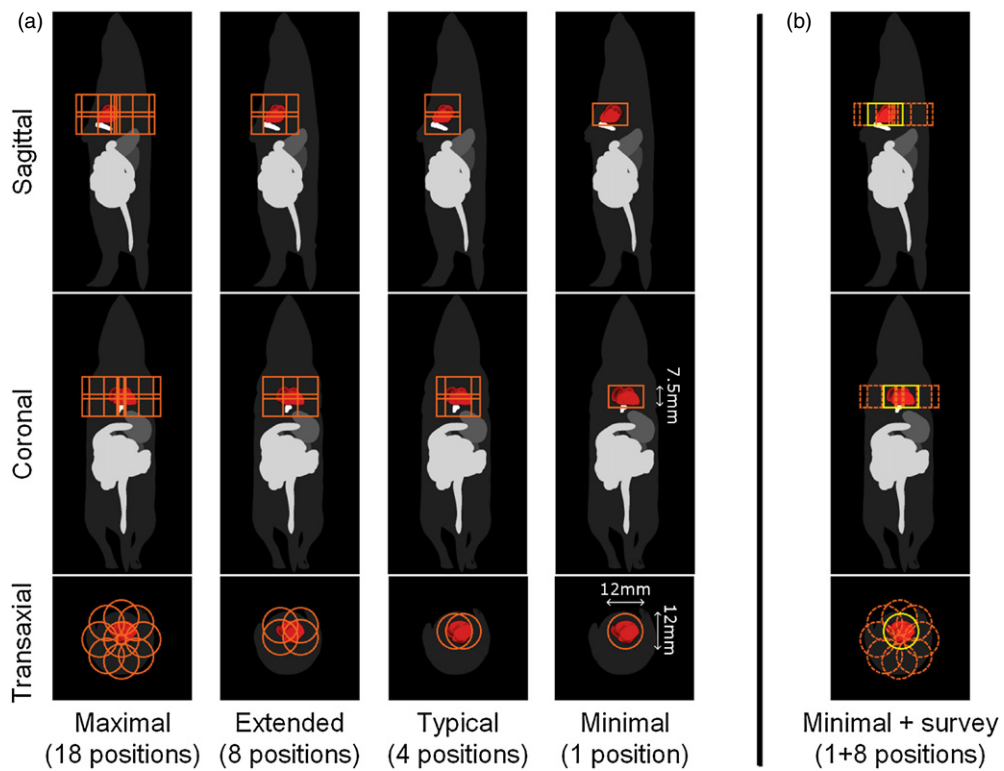
Figure 2. (a) CFOV locations overlaid onto maximum-intensity projections of the phantom for various scan protocols with increasing level of truncation. From top to bottom: sagittal view, coronal view, transaxial view. Heart is shown in red for clarity. (b) Like (a) but for minimal scan protocol with survey scan. Solid line denotes main CFOV location and dashed lines denote exterior CFOV locations that are scanned only shortly.
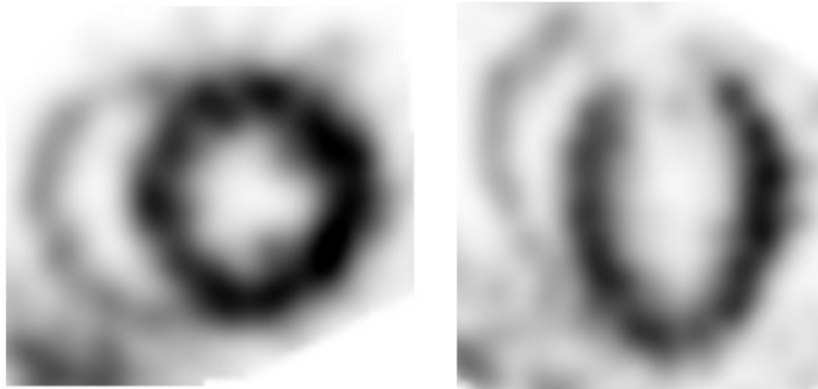

Figure 3. Typical images from example ECG-gated ^{99m}Tc-tetrofosmin U-SPECT-II scan of mouse heart in end-diastole, showing myocardial perfusion even in papillary muscles and right ventricular wall.

computing one forward projection for each bed position. The same system matrix can be used for all bed positions by restricting all bed shifts to an integer times the voxel size (Vastenhouw and Beekman 2007).

2.5. Image reconstruction

Images were reconstructed using pixel-based ordered subset expectation maximization (POSEM) incorporating an accurate system matrix (van der Have *et al* 2008). POSEM iteratively updates the activity estimate according to Hudson and Larkin (1994) but using a subset choice that is more robust than standard OSEM for multipinhole SPECT reconstruction, in particular when high acceleration factors are used (Branderhorst *et al* 2010). Reconstructions were performed on a 0.1875 mm isotropic voxel grid, using a system matrix that was different from the matrix used for simulating the acquisitions (which was based on 0.09375 mm isotropic voxels). This approximately simulates the continuous character of real data. A total of 36 POSEM iterations with 16 subsets were used for all reconstructions in this study, with the start image set to a uniformly filled cylinder with inner diameter 26 mm (which equals the diameter of the animal bed) and length 29.25 mm (which equals the length of the system matrix support in the Z (longitudinal) direction).

2.6. Image assessment

To investigate the influence of truncated projections on (pre)clinical myocardial perfusion scoring, the results were assessed visually by inspecting short-axis slices (slice thickness 0.375 mm) with corresponding maximum-count circumferential profiles. In addition, 2D polar maps were constructed. All image volumes were reoriented, resampled using trilinear interpolation, and then smoothed using an isotropic 3D Gaussian kernel with $\sigma = 0.28$ mm except for the low-count images, which were smoothed with $\sigma = 0.32$ mm. The Gaussian kernel parameters were chosen such that the lesions were still clearly visible. The same procedure of reorienting, resampling, and smoothing with $\sigma = 0.28$ mm was applied also directly to the phantom, in order to obtain a true image that was used to judge whether the reconstruction obtained with the maximal scan protocol replicated the phantom accurately enough to be used as a gold standard. Circumferential profiles were automatically generated using a distance-weighted two-part sampling scheme that samples the basal part of the myocardium cylindrically, and the apical part spherically (Garcia *et al* 1990). The 2D polar ('bull's eye') maps were constructed by mapping sequential circumferential profiles, extending from the apex to the base, into successive rings on the polar map. Differences in the polar maps between each reconstructed image and the gold standard (the maximal FOV selection) were calculated for the mean pixel values in the 17 standardized myocardial segments shown in figure 4.

3. Results

Figure 5 shows that there is an influence of truncated extra-cardiac activity on the reconstructed myocardium. When performing simulations with surrounding activity present, the myocardial activity reconstructed using the minimal scan protocol is negatively biased and the resulting short-axis slice and bull's eye plot are significantly distorted, compared to the maximal and true phantom images. However, when performing the same simulations on the myocardial activity only, with all other activity set to zero, the minimal, maximal and true images are mutually nearly identical, and almost equal to the maximal and true phantom images obtained from the
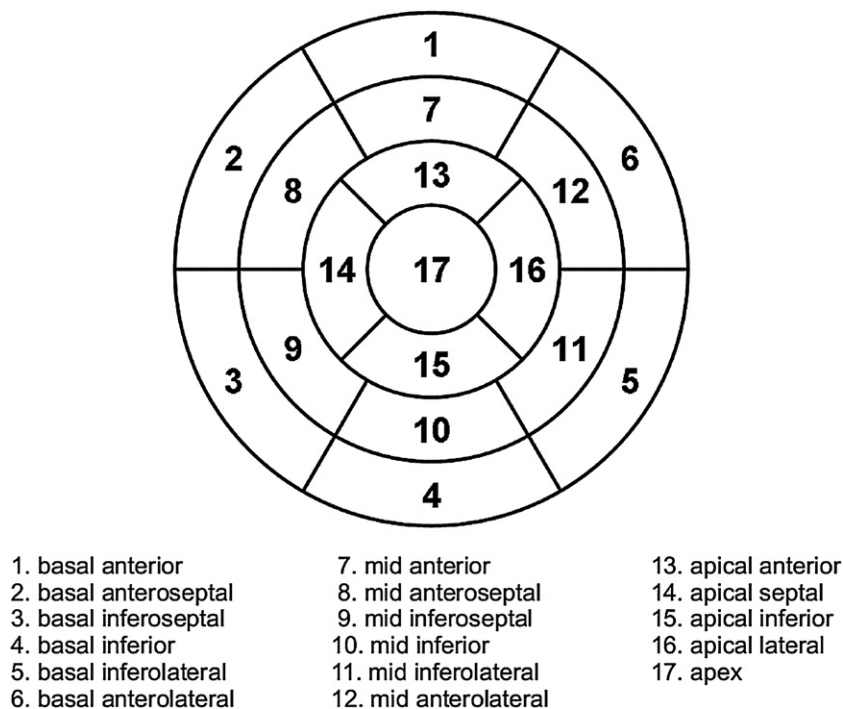
Figure 4. Display, on a circumferential polar plot, of the 17 myocardial segments as recommended in Cerqueira *et al* (2002).

complete phantom. This clearly demonstrates that the distortions in the images obtained with the minimal scan volume are caused predominantly by the surrounding activity, whereas the influence of other parameters such as differences in angular sampling is minimal.

The reconstruction obtained with the maximal scan volume is very similar to the corresponding true phantom image, both with and without extra-cardiac activity present. This supports its use as a gold standard which, compared to using the true phantom image directly, has the advantage that it anticipates deviations due to inaccurate system modelling and round-off errors during reconstruction.

Figures 6–8 illustrate the effect of varying the level of truncation on the reconstructed activity in the left ventricular myocardium. Figure 6 shows that the noiseless images obtained with the extended and typical protocols appear visually almost identical to the gold standard, although the right ventricular wall appears slightly thinner in the typical case. The minimal protocol, introducing the highest degree of truncation, produced strong visual distortions in the noiseless reconstructed images. These distortions disappeared almost completely when the minimal protocol was augmented with the survey scan. Figure 7 demonstrates that the reconstructions become more negatively biased when the level of truncation is increased. However, the different results obtained at the various truncation levels were very similar after normalization to the mean of the gold standard (the maximal protocol).

The bull's eye plots in figure 8 show that these observations also apply to other parts of the myocardium. The corresponding quantitative data in table 2 report that the results obtained with the minimal + survey scan protocol were the closest to the gold standard, with average and maximum deviations of respectively 1.8% and 4.4%. This is also reflected in figures 6 and 8, in which the noiseless minimal + survey images are visually the most similar to the gold standard.
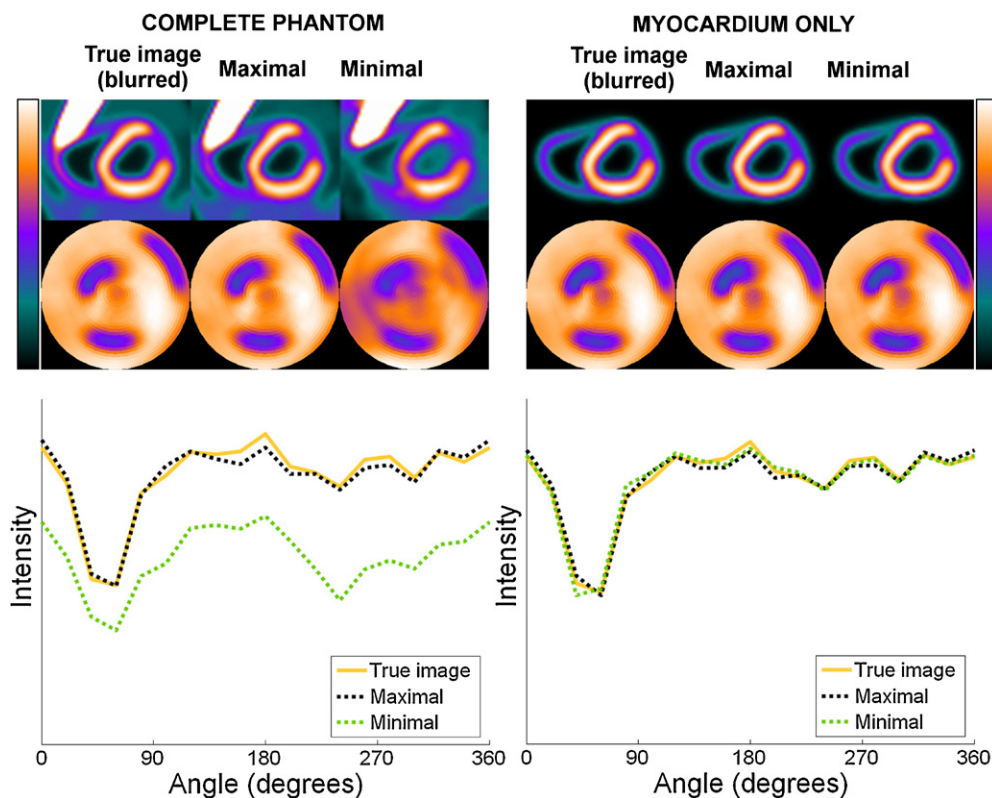
Figure 5. Short-axis slices (top), bull's eye plots (middle) and circumferential profiles (bottom) of slightly blurred true phantom image (left) and of images obtained from noise-free simulations using maximal and minimal scan protocols (middle and right). Left: simulations with complete phantom showing distortion for minimal FOV selection. Right: simulations with all extra-cardiac activity set to zero showing no distortion when the selected area is very small.

The observations made from the noiseless images in figure 6 seem to apply also to the noisy images, although the truncation effects are less evident because of the noise artefacts, especially in the low-count images. Figure 7 shows that when averaged, the noisy profiles show a negative general bias depending on the degree of truncation, which is similar to the noiseless case. Furthermore, the average noisy profiles resulting from the different scan protocols are again very similar after normalization.

For low-count noisy projection data, table 3 shows that the typical protocol produced bull's eye plots that were on average the most similar to the gold standard (the noiseless maximal protocol), with average and maximum deviations of respectively 3.2% and 10.0%. Interestingly, these deviations are even lower than those measured for the minimal + survey protocol. It should also be noted that even the protocol with the maximum field-of-view resulted in small average and maximal deviations from the gold standard, which suggests that the deviations reported for the noisy case may be at least partly caused by noise.

4. Discussion

We have investigated the influence of extra-cardiac activity on the reconstruction of myocardial uptake distributions in a focusing multipinhole SPECT geometry. Our results demonstrate that
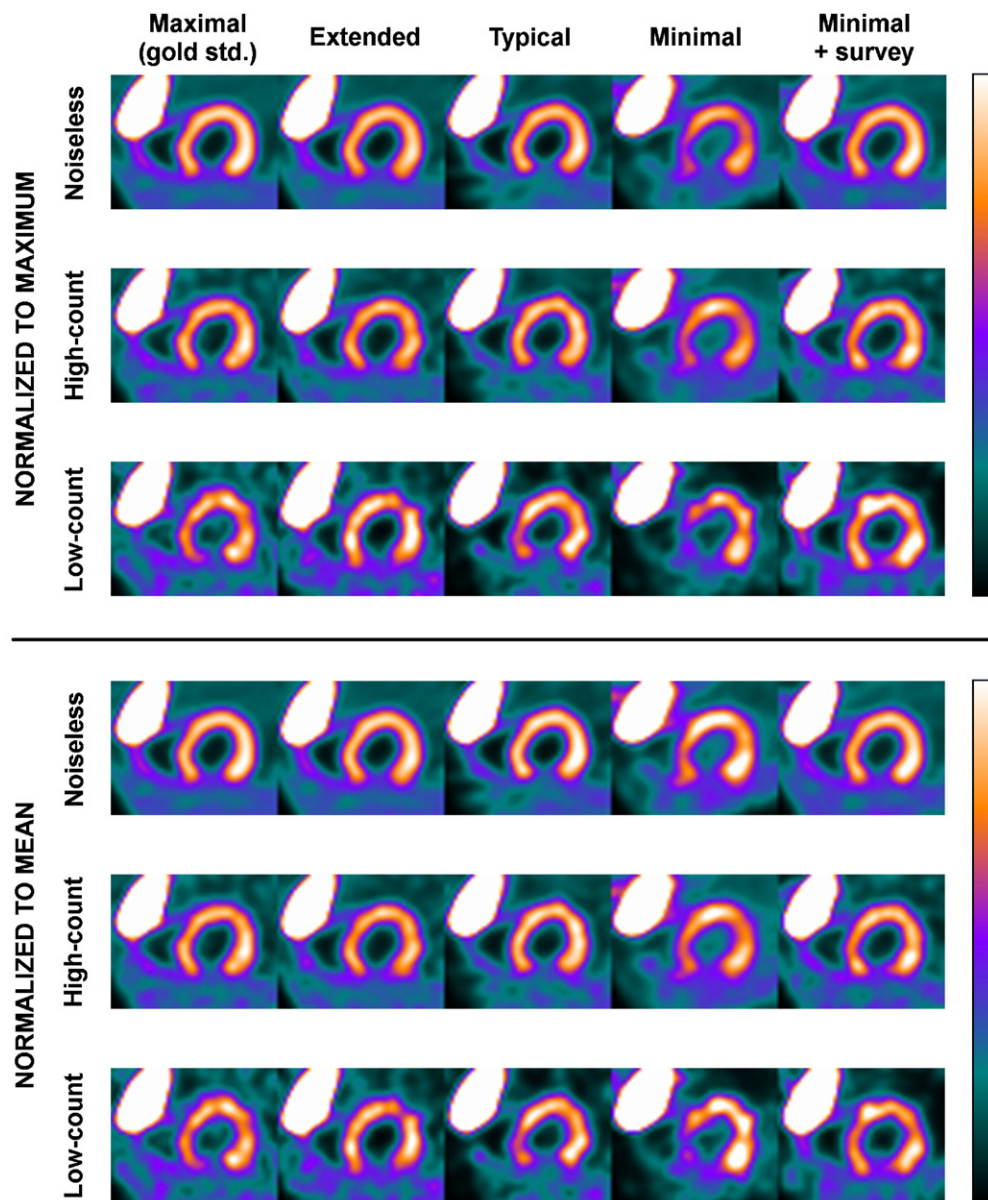
Figure 6. Representative reconstructed short-axis slices for each of the five scan protocols, with infarct visible in inferior myocardium. Top: noiseless, high-count noisy and low-count noisy images normalized to myocardial maximum. Bottom: same as top but normalized to myocardial mean.

if extra-cardiac activity is truncated from the acquired projections, the amount of reconstructed myocardial uptake is negatively biased depending on the degree of truncation. This finding is consistent with previous literature (Zeng *et al* 2010). The bias appears to be approximately constant over the entire myocardium and the differences between the reconstructions obtained with various levels of truncation largely disappear after normalization to the mean myocardial activity.
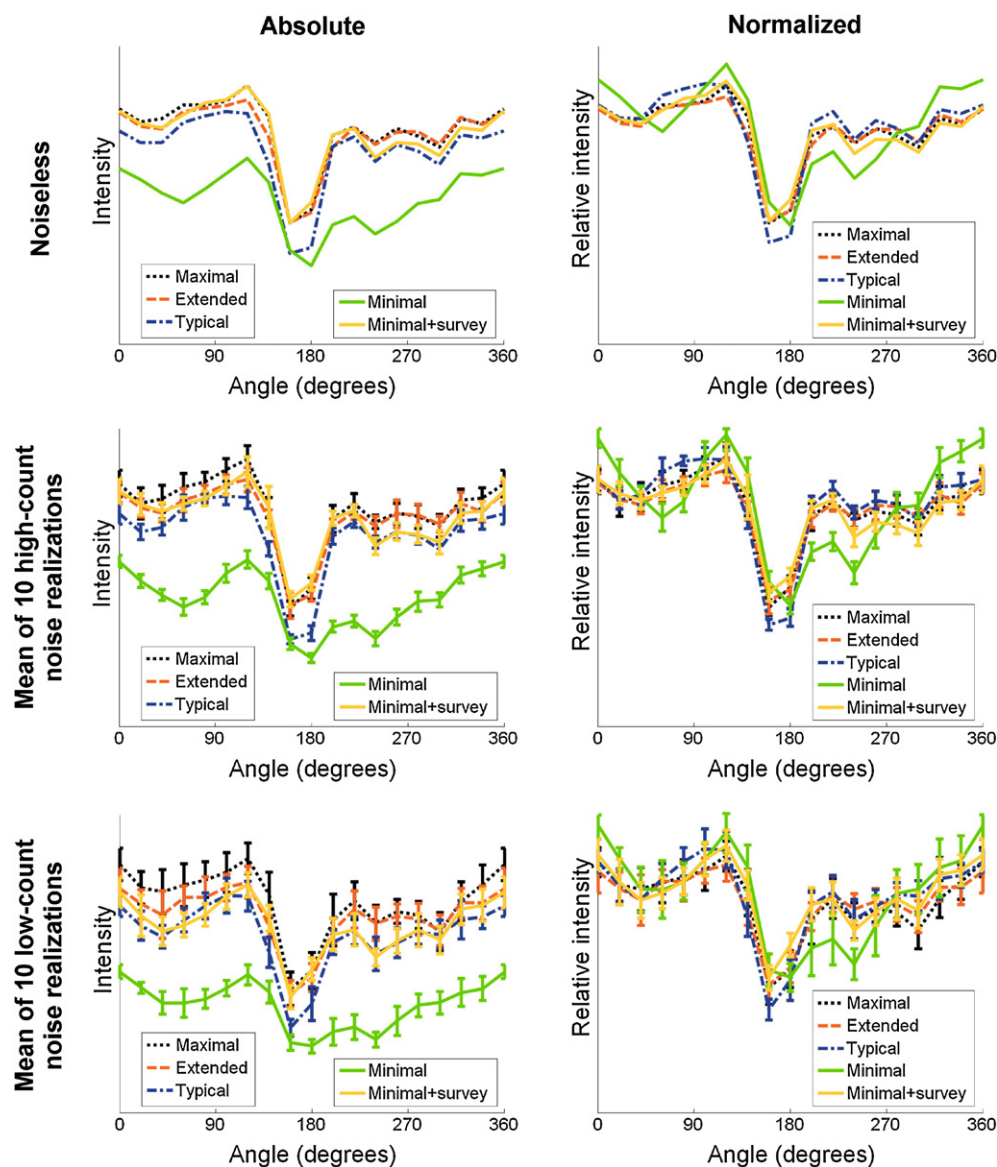
Figure 7. Circumferential profiles corresponding to reconstructed slices shown in figure 6. Left: absolute values. Right: values normalized to myocardial mean. Top: noiseless reconstructions. Middle: Averaged from ten noisy simulations with error bars representing standard error. Bottom: like middle row but for noisy simulations with only one-fourth of the counts.

We have also explored the possibility of reducing the bias by sacrificing a small part of the scan time to perform a short survey scan of the truncated activity. Although this strategy produced the best results in the noiseless simulations, in the presence of noise the survey scan seems to be less effective in reducing the truncation bias, even after a very high number of OS-EM iterations. A possible cause may be that if the number of counts acquired in a survey scan is below a certain threshold, its reconstruction is dominated too much by noise artefacts to allow an accurate truncation bias correction. Yet, in our low-count simulations the survey
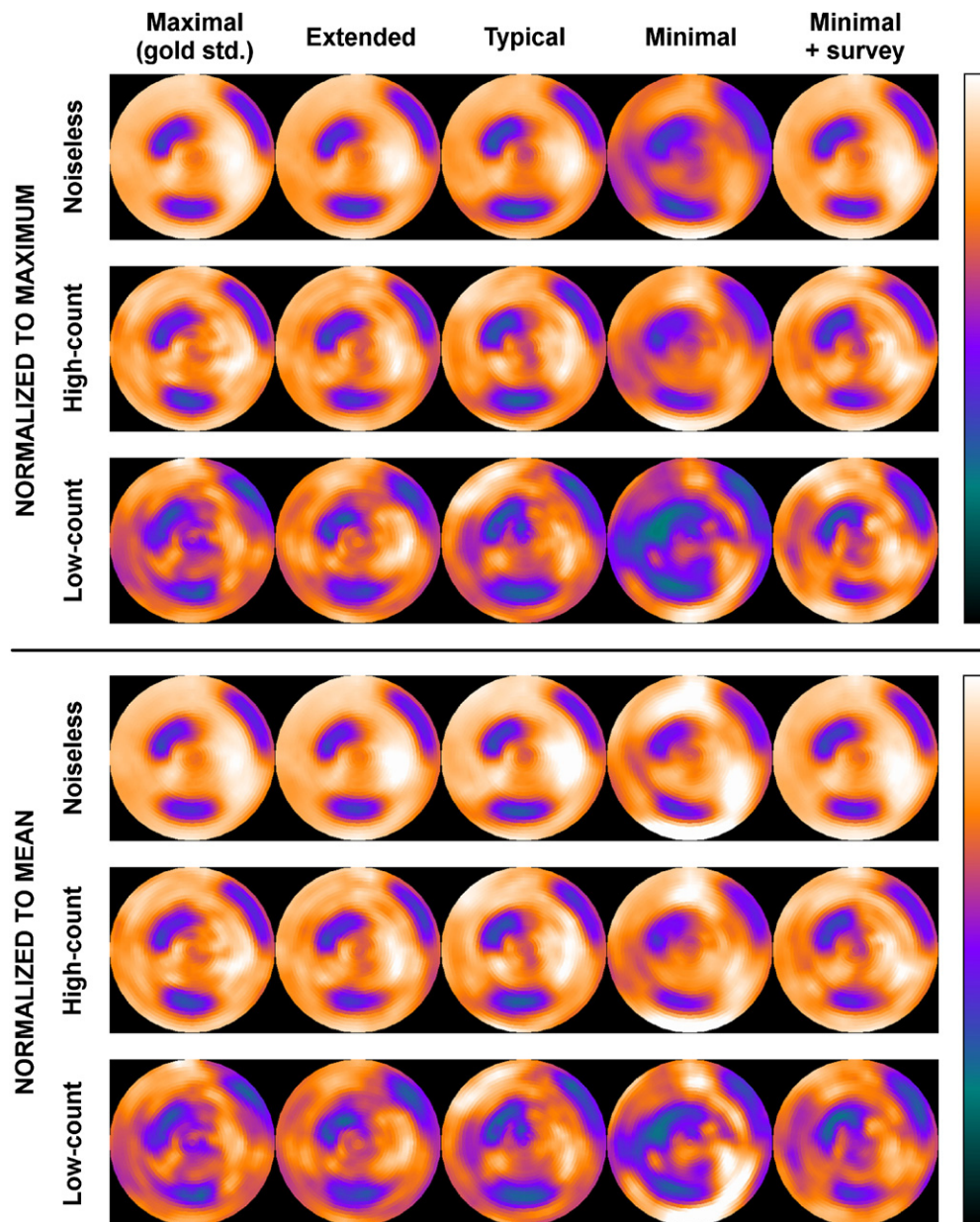
Figure 8. Bull's eye plots for each of the five scan protocols. Top: noiseless, high-count noisy and low-count noisy images normalized to myocardial maximum. Bottom: same as top but normalized to myocardial mean.

scan was still able to reduce approximately 75% of the difference in reconstructed uptake between the highest and the lowest levels of truncation.

An alternative method to reduce artefacts resulting from local tomography and truncated projections is employing a support prior (Manglos *et al* 1993). However, this method makes the reconstructions dependent on the user-defined size and shape of the support prior. Our proposed method of using a fast survey scan is more robust since its correction is automatically adapted

Table 2. Differences in noiseless bull's eye plot myocardial regions between maximal protocol (gold standard) and all other scan protocols. Values shown are deviations in average pixel-counts expressed as a percentage of the average pixel-counts in the corresponding region in the gold standard. All bull's eye plots were first normalized to their myocardial mean. Maximum absolute percentage differences are marked in bold italics.

	Extended	Typical	Minimal	Minimal + survey
1. Basal anterior	0.7%	1.4%	2.9%	0.6%
2. Basal anteroseptal	1.3%	2.2%	−4.2%	0.3%
3. Basal inferoseptal	−1.4%	−3.6%	−5.3%	2.1%
4. Basal inferior	1.5%	−3.5%	***18.6%***	3.4%
5. Basal inferolateral	***−5.2%***	−2.9%	−0.6%	0.3%
6. Basal anterolateral	−1.1%	1.5%	1.5%	1.4%
7. Mid-anterior	1.6%	3.1%	12.1%	−0.4%
8. Mid-anteroseptal	3.3%	1.4%	−1.7%	−2.6%
9. Mid-inferoseptal	−0.1%	2.6%	−14.9%	−0.2%
10. Mid-inferior	−3.4%	***−9.0%***	10.9%	2.1%
11. Mid-inferolateral	−1.1%	1.4%	2.7%	2.1%
12. Mid-anterolateral	−2.3%	0.9%	−9.2%	−2.3%
13. Apical anterior	2.5%	0.1%	2.2%	***−4.4%***
14. Apical septal	−1.1%	2.3%	−3.2%	−4.3%
15. Apical inferior	−0.6%	−1.3%	1.4%	1.4%
16. Apical lateral	3.7%	3.0%	−4.0%	0.8%
17. Apex	0.7%	−2.5%	−6.1%	−1.5%
Mean absolute deviation	1.9%	2.5%	6.0%	1.8%

Table 3. Like table 2 but showing deviations per region averaged over ten noisy low-count simulations, using noiseless maximal protocol as gold standard.

	Maximal	Extended	Typical	Minimal	Minimal + survey
1. Basal anterior	−0.2%	2.3%	3.9%	7.0%	3.0%
2. Basal anteroseptal	−1.2%	−0.5%	3.7%	0.0%	0.5%
3. Basal inferoseptal	−1.6%	0.6%	−5.8%	−10.2%	3.0%
4. Basal inferior	1.8%	2.3%	−2.0%	***28.4%***	***12.5%***
5. Basal inferolateral	1.7%	***−4.3%***	0.0%	6.0%	−0.1%
6. Basal anterolateral	4.1%	−2.0%	0.4%	−5.9%	−4.9%
7. Mid-anterior	3.4%	1.9%	5.5%	11.6%	5.8%
8. Mid-anteroseptal	***−4.2%***	2.5%	2.9%	−0.6%	2.1%
9. Mid-inferoseptal	−2.4%	−1.2%	2.4%	−21.5%	−0.1%
10. Mid-inferior	0.5%	0.1%	***−10.0%***	7.1%	6.2%
11. Mid-inferolateral	−0.2%	−0.8%	2.5%	4.4%	1.4%
12. Mid-anterolateral	0.1%	−2.6%	−1.2%	−6.5%	−7.5%
13. Apical anterior	0.3%	2.7%	−0.8%	−1.8%	−4.8%
14. Apical septal	2.7%	−1.7%	−0.9%	−10.7%	−6.1%
15. Apical inferior	−1.1%	−0.4%	−0.4%	−3.3%	−3.6%
16. Apical lateral	1.0%	3.3%	3.1%	−1.3%	−1.7%
17. Apex	−3.5%	−2.8%	−8.3%	−8.3%	−8.7%
Mean absolute deviation	1.8%	1.9%	3.2%	7.9%	4.2%

to the activity distribution of each scan individually. Another advantage is that when the survey scan is performed first, it can also be used for scan planning of the main scan.

In our simulations we accurately modelled distance-dependent detector response and sensitivity, as it is very accurately incorporated into the system matrix that was used for simulation. The small contribution of scatter (5–10% (Meikle *et al* 2005, Vanhove *et al* 2009,

Chen *et al* 2009)) that is present in ^{99m}Tc projections of small objects such as mice, which we normally correct with the triple-energy-window method was not modelled in the projection and therefore no correction for this effect was applied either. By both not modelling and not correcting for detected scatter we minimize the already small bias with real (measured) data. Attenuation was not modelled since it is complex to combine with a realistic measured system matrix. Effects of attenuation in mice at 140 keV are small however: when assuming a conservative average photon path length of 1 cm water, the amount of attenuation is <14%. This relatively small effect, compared to attenuation in humans, results only in a small quite global decrease of activity, and a relatively simple Chang correction was proven to be quite accurate for ^{99m}Tc, even in larger rodents such as rats (Wu *et al* 2010). However, since we did not model attenuation during simulation we did not correct for it either to minimize the net difference between simulation and reality. As a result, our study accurately mimics images that are corrected for attenuation and scatter with commercially available correction methods (Chang 1978, Ogawa *et al* 1991, Wu *et al* 2010). Due to count losses caused by attenuation and count increase resulting from detection of scatter, the simulations performed in this study underestimate the number of detected photons by about 4–9%. This global underestimation may slightly affect the image noise, but we assume that it has a negligible effect on the reported errors in the myocardium due to extra-cardiac activity.

Since our simulation employed a static tracer distribution, the sampling of the exterior bed positions during the survey scan was always consistent with the appearance of the exterior activity in the projections of the heart. In the case of quickly changing tracer kinetics, the exterior activity may need to be scanned once for each time frame. On the other hand, for a long static scan of a slowly changing but dynamic distribution, a good truncation correction may be obtained using the average of one pre- and one post-scan of the exterior activity.

In this research, the application under study was myocardial perfusion scanning using a preclinical focusing multipinhole SPECT scanner. Although this is a rather specific application, our results and recommendations may be generalized to other scan types where uptake outside the organ of interest is a concern, such as tumour studies, kidney scans and investigations of the gastro-intestinal tract. In addition, an increasing number of preclinical and clinical scanners employ a focusing multipinhole SPECT design to obtain increased sensitivity and resolution (e.g. Beekman and van der Have 2007, Funk *et al* 2006a, 2006b, DiFilippo 2008, Vunckx *et al* 2009, Shokouhi *et al* 2009, Huang *et al* 2007, Goorden *et al* 2009, Bocher *et al* 2010).

5. Conclusion

Our results indicate that in focused multipinhole SPECT, the reconstructed tracer distribution in the myocardium is influenced by high activity in surrounding organs, and imaging tasks that rely on absolute quantification may be adversely affected. However, the classification of myocardial infarcts is influenced only slightly for typical scan volumes as long as the results are normalized to the mean myocardial activity. Influence of external tracer uptake can be reduced by extending the scan volume in the transaxial directions using a very short additional survey scan.

Acknowledgments

References

Amano S, Inoue T, Tomiyoshi K, Ando T and Endo K 1998 *In vivo* comparison of PET and SPECT radiopharmaceuticals in detecting breast cancer *J. Nucl. Med.* **39** 1424–7

Baiker M, Vastenhouw B, Branderhorst W, Reiber J H C, Beekman F and Lelieveldt B P F 2009 Atlas-driven scan planning for high-resolution micro-SPECT data acquisition based on multi-view photographs: a pilot study *Proc. of SPIE Medical Imaging 2009 (Lake Buena Vista, FL, USA)* p 72611L (8 p)

Beekman F J 2004 Method of obtaining a tomographic image *Patent:* US2004149923 (A1)-2004-08-05. Priority Date: 2001-05-11

Beekman F J, van der Have F, Vastenhouw B, van der Linden A J A, van Rijk P P, Burbach J P H and Smidt M P 2005 U-SPECT-I: a novel system for submillimeter-resolution tomography with radiolabeled molecules in mice *J. Nucl. Med.* **46** 1194–200

Beekman F J and van der Have F 2007 The pinhole: gateway to ultra-high-resolution three-dimensional radionuclide imaging *Eur. J. Nucl. Med. Mol. Imaging* **34** 151–61

Beekman F J, Vastenhouw B, van der Wilt G, Vervloet M, Visscher R, Booij J, Gerrits M, Ji C, Ramakers R and van der Have F 2009 3-D rat brain phantom for high-resolution molecular imaging *Proc. IEEE* **97** 1997–2005

Bocher M, Blevis I M, Tsukerman L, Shrem Y, Kovalski G and Volokh L 2010 A fast cardiac gamma camera with dynamic SPECT capabilities: design, system validation and future potential *Eur. J. Nucl. Med. Mol. Imaging* **37** 1887–902

Branderhorst W, Vastenhouw B and Beekman F J 2010a Pixel-based subsets for rapid multi-pinhole SPECT reconstruction *Phys. Med. Biol.* **55** 2023–34

Branderhorst W, Vastenhouw B, van der Have F, Blezer E L A, Bleeker W K and Beekman F J 2010b Targeted multi-pinhole SPECT *Eur. J. Nucl. Med. Mol. Imaging* **38** 552–61

Cerqueira M D, Weissman N J, Dilsizian V, Jacobs A K, Kaul S, Laskey W K, Pennell D J, Rumberger J A, Ryan T and Verani M S 2002 Standardized myocardial segmentation and nomenclature for tomographic imaging of the heart: a statement for healthcare professionals from the Cardiac Imaging Committee of the Council on Clinical Cardiology of the American Heart Association *Circulation* **105** 539–42

Chang L-T 1978 A method for attenuation correction in radionuclide computed tomography *IEEE Trans. Nucl. Sci.* **25** 638–43

Chen C-L, Wang Y, Lee J J S and Tsui B M W 2009 Toward quantitative small animal pinhole SPECT: assessment of quantitation accuracy prior to image compensations *Mol. Imaging Biol.* **11** 195–203

Clackdoyle R and Defrise M 2010 Tomographic reconstruction in the 21st century *IEEE Signal Proc. Mag.* **27** 60–80

Clackdoyle R, Noo F, Guo J and Roberts J A 2004 Quantitative reconstruction from truncated projections in classical tomography *IEEE Trans. Nucl. Sci.* **51** 2570–8

DiFilippo F P 2008 Design and performance of a multi-pinhole collimation device for small animal imaging with clinical SPECT and SPECT-CT scanners *Phys. Med. Biol.* **53** 4185–201

Franc B L, Acton P D, Mari C and Hasegawa B H 2008 Small-animal SPECT and SPECT/CT: important tools for preclinical investigation *J. Nucl. Med.* **49** 1651–63

Funk T, Després P, Barber W C, Shah K S and Hasegawa B H 2006a A multipinhole small animal SPECT system with submillimeter spatial resolution *Med. Phys.* **33** 1259–68

Funk T, Kirch D L, Koss J E, Botvinick E and Hasegawa B H 2006b A novel approach to multipinhole SPECT for myocardial perfusion imaging *J. Nucl. Med.* **47** 595–602

Garcia E V *et al* 1990 Technical aspects of myocardial spect imaging with technetium-99m sestamibi *Am. J. Cardiol.* **66** E23–31

Golestani R, Wu C, Tio R A, Zeebregts C J, Petrov A D, Beekman F J, Dierckx R A J O, Boersma H H and Slart R H J A 2010 Small-animal SPECT and SPECT/CT: application in cardiovascular research *Eur. J. Nucl. Med. Mol. Imaging* **37** 1766–77

Goorden M C, Rentmeester M C M and Beekman F J 2009 Theoretical analysis of full-ring multi-pinhole brain SPECT *Phys. Med. Biol.* **54** 6593–610

Gregoriou G K, Tsui B M W, Frey E C and Lalush D S 1995 Artifacts and sampling requirement in transmission CT reconstruction with truncated projection data *Nuclear Science Symp. and Medical Imaging Conf. Record (San Francisco, CA, USA)* vol 3 pp 1336–40

Hoffman J M and Gambhir S S 2007 Molecular imaging: the vision and opportunity for radiology in the future *Radiology* **244** 39–47

Huang Q, Boutchko R, Reutter B and Gullberg G 2007 Dynamic imaging with a novel dedicated cardiac SPECT system *J. Nucl. Med.* **50** 525 Suppl 2

Hudson H M and Larkin R S 1994 Accelerated image reconstruction using ordered subsets of projection data *IEEE Trans. Med. Imaging* **13** 601–9

Kadrmas D J, Jaszczak R J, McCormick J W, Coleman R E and Lim C B 1995 Truncation artifact reduction in transmission CT for improved SPECT attenuation compensation *Phys. Med. Biol.* **40** 1085–104

King M A, Pretorius P H, Farncombe T and Beekman F J 2002 Introduction to the physics of molecular imaging with radioactive tracers in small animals *J. Cell. Biochem. Suppl.* **39** 221–30

Lalush D S and Tsui B M W 2000 Performance of ordered-subset reconstruction algorithms under conditions of extreme attenuation and truncation in myocardial SPECT *J. Nucl. Med.* **41** 737–44

Maass P 1992 The interior radon transform *SIAM J. Appl. Math.* **52** 710–24

Manglos S H, Gagne G M and Bassano D A 1993 Quantitative analysis of image truncation in focal-beam CT *Phys. Med. Biol.* **38** 1443–57

Massoud T F and Gambhir S S 2003 Molecular imaging in living subjects: seeing fundamental biological processes in a new light *Gene. Dev.* **17** 545–80

Meikle S R, Kench P, Kassiou M and Banati R B 2005 Small animal SPECT and its place in the matrix of molecular imaging technologies *Phys. Med. Biol.* **50** R45–61

Ogawa K, Harata Y, Ichihara T, Kubo A and Hashimoto S 1991 A practical method for position-dependent Compton-scatter correction in single photon emission CT *IEEE Trans. Med. Imaging* **10** 408–12

Pysz M A, Gambhir S S and Willmann J K 2010 Molecular imaging: current status and emerging strategies *Clin. Radiol.* **65** 500–16

Rowland D J and Cherry S R 2008 Small-animal preclinical nuclear medicine instrumentation and methodology *Semin. Nucl. Med.* **38** 209–22

Segars W P, Tsui B M W, Frey Eric C, Johnson G A and Berr S S 2004 Development of a 4-D digital mouse phantom for molecular imaging research *Mol. Imaging Biol.* **6** 149–59

Shokouhi S, Metzler S D, Wilson D W and Peterson T E 2009 Multi-pinhole collimator design for small-object imaging with SiliSPECT: a high-resolution SPECT *Phys. Med. Biol.* **54** 207–25

Tsui B M W and Kraitchman D L 2009 Recent advances in small-animal cardiovascular imaging *J. Nucl. Med.* **50** 667–70

Vaissier P E, Goorden M C, van der Have F, Vastenhouw B and Beekman F J 2010 Fast whole-body mouse imaging with a stationary multi-pinhole SPECT system using spiral bed trajectories *Proc. of the 4th Biannual Workshop on Small Animal SPECT Imaging*

van der Have F, Vastenhouw B, Ramakers R M, Branderhorst W, Krah J O, Ji C, Staelens S G and Beekman F J 2009 U-SPECT-II: an ultra-high-resolution device for molecular small-animal imaging *J. Nucl. Med.* **50** 599–605

van der Have F, Vastenhouw B, Rentmeester M and Beekman F J 2008 System calibration and statistical image reconstruction for ultra-high resolution stationary pinhole SPECT *IEEE Trans. Med. Imaging* **27** 960–71

Vanhove C, Defrise M, Bossuyt A and Lahoutte T 2010 Improved quantification in multiple-pinhole SPECT by anatomy-based reconstruction using microCT information *Eur. J. Nucl. Med. Mol. Imaging* **38** 153–65

Vanhove C, Defrise M, Bossuyt A and Lahoutte T 2009 Improved quantification in single-pinhole and multiple-pinhole SPECT using micro-CT information *Eur. J. Nucl. Med. Mol. Imaging* **36** 1049–63

Vastenhouw B and Beekman F 2007 Submillimeter total-body murine imaging with U-SPECT-I *J. Nucl. Med.* **48** 487–93

Vastenhouw B, van der Have F, van der Linden A J A, von Oerthel L, Booij J, Burbach J P H, Smidt M P and Beekman F J 2007 Movies of dopamine transporter occupancy with ultra-high resolution focusing pinhole SPECT *Mol. Psychiatr.* **12** 984–7

Vunckx K, Nuyts J, Vanbilloen B, De Saint-Hubert M, Vanderghinste D, Rattat D, Mottaghy F M and Defrise M 2009 Optimized multipinhole design for mouse imaging *IEEE Trans. Nucl. Sci.* **56** 2696–705

Wiesmann F *et al* 2001 Dobutamine-stress magnetic resonance microimaging in mice: acute changes of cardiac geometry and function in normal and failing murine hearts *Circ. Res.* **88** 563–9

Wu C, van der Have F, Vastenhouw B, Dierckx R A J O, Paans A M J and Beekman F J 2010 Absolute quantitative total-body small-animal SPECT with focusing pinholes *Eur. J. Nucl. Med. Mol. Imaging* **37** 2127–35

Xiao J, Verzijlbergen F J, Viergever M A and Beekman F J 2010 Small field-of-view dedicated cardiac SPECT systems: impact of projection truncation *Eur. J. Nucl. Med. Mol. Imaging* **37** 528–36

Zeng G L and Gullberg G T 1990 A study of reconstruction artifacts in cone beam tomography using filtered backprojection and iterative EM algorithms *IEEE Trans. Nucl. Sci.* **37** 759–67

Zeng G L, Gullberg G T and Kadrmas D J 2010 Closed-form kinetic parameter estimation solution to the truncated data problem *Phys. Med. Biol.* **55** 7453–68

Zhang B and Zeng G L 2007 Two-dimensional iterative region-of-interest (ROI) reconstruction from truncated projection data *Med. Phys.* **34** 935–44